The Effects of Non-Inhibitory Serpin Maspin on the Actin Cytoskeleton: A Quantitative Image Modelling Approach

Mohammed Al-Mamun[1,2,3], Lorna Ravenhill[1,4], Worawut Srisukkham[2], Alamgir Hossain[2,5], Charles Fall[2], Vincent Ellis[4] & Rosemary Bass[6]

[1] These authors contributed equally

[2] Computational Intelligence Group, Faculty of Engineering and Environment, Northumbria University, UK

[3] Department of Population Medicine & Diagnostic Sciences, College of Veterinary Medicine, Cornell University, Ithaca, NY 14850, USA

[4] School of Biological Sciences, University of East Anglia, Norwich, Norfolk, NR4 7TJ, UK

[5] Anglia Ruskin IT Research Institute (ARITI), Anglia Ruskin University, Cambridge, CB1 1PT, UK

[6] Department of Applied Sciences, Faculty of Health and Life Sciences, Northumbria University, Newcastle upon Tyne, NE1 8ST, UK. Corresponding author: rosemary.bass@northumbria.ac.uk, telephone +44 (0)191 2274899, no fax number.

Running Title – Modelling maspin effects on the cytoskeleton

Key words/phrases – SerpinB5, Cell migration, Quantitative image modelling, Watershed segmentation, Confocal Microscopy, Phalloidin

ABSTRACT

Recent developments in quantitative image analysis allow us to interrogate confocal microscopic images to answer biological questions. Clumped and layered cell nuclei and cytoplasm in confocal microscopic images challenges the ability to identify subcellular compartments. To date, there is no perfect image analysis method to identify cellular cytoskeletal changes from confocal microscopic images. Here we present a multi-disciplinary study where an image analysis model was developed to allow quantitative measurements of changes in the cytoskeleton of cells with different maspin exposure. Maspin, a non-inhibitory serpin influences cell migration, adhesion, invasion, proliferation and apoptosis in ways that are consistent with its identification as a tumor metastasis suppressor. Using different cell types we tested the hypothesis that the reduction of cell migration by maspin would be reflected in the architecture of the actin cytoskeleton. A hybrid marker controlled watershed segmentation technique was used to segment the nuclei, cytoplasm and ruffling regions prior to measuring cytoskeletal changes. This was informed by immunohistochemical staining of cells transfected stably or transiently with maspin proteins, or with added bioactive peptides or protein. Image analysis results showed that the effects of maspin were mirrored by effects on cell architecture, in a way that could be described quantitatively.

INTRODUCTION

Here we present a novel quantitative image analysis model allowing the description and quantitation of cell morphology from the image analysis of the actin cytoskeleton. We have generated image data from cells with varying exposure to tumor suppressive maspin (SerpinB5), a non-inhibitory serpin which reduces cell migration and alters cellular cytoskeletal morphology. Maspin has been widely reported to be a tumor metastasis suppressor that can influence multiple cellular functions (reviewed by Bodenstine *et al.* 2012). In addition to regulating cell migration, maspin can increase adhesion and the tendency to undergo apoptosis, as well as decreasing proliferation and angiogenesis. Maspin is expressed by normal cell types including epithelial cells, and is lost in the pathogenesis of cancer. We have previously demonstrated that maspin influences vascular smooth muscle cell (VSMC) adhesion and migration (Bass *et al.* 2002, 2009, Ravenhill *et al.* 2010); behaviours critical in the build-up of atherosclerotic plaques. We have previously reported an *in silico* model of how the presence or absence of maspin influences the growth and behaviour of tumors (Al-Mamun *et al.* 2013). This model was enriched by data from *in vitro* experiments, as well as building on previous mathematical models. Here, we investigate the effects of maspin on the cellular cytoskeleton during tumor growth from the subcellular point of view. The image analysis model employed the input image samples, a segmentation method and quantitative measures of segmented cell parts (nuclei, cytoplasm and ruffling region) to investigate the hypotheses. We report the development of a hybrid approach of marker controlled watershed segmentation algorithm, which allowed us to segment confocal microscopy images into interested parts (i.e. nuclei, cytoplasm and ruffling regions) and measure quantitative parameters of cell shape and morphology for comparison with visual inspection and measured cell behaviours.

There are many reports indicating that maspin can influence the behaviour of a range of cell types, such that generally maspin expressing cells are more adherent and less migratory (Bodenstine *et al.* 2012). It would be anticipated that these functions of maspin are reflected by the morphology of the actin cytoskeleton of cells. The cytoskeleton in a non-migratory cell is typified by well established, elongated, thick actin filaments; in comparison to migratory cells which have short filaments and more lamellipodia (Ridley *et al.* 2003). Maspin has indeed been linked to remodelling of the actin cytoskeleton in models of breast (Odero-Marah *et al.* 2003) and ovarian (Lara *et al.* 2012) cancer, in addition to endothelial cells (Qin & Zhang 2010).

We have previously demonstrated that the effects of full length maspin and the isolated G α-helix (G-helix) on cell migration are reflected in changes in the actin cytoskeleton (Ravenhill *et al.* 2010). The G-helix motif unique to maspin orthologues is essential and sufficient for the reduction of cell migration by maspin. Single point mutation of either of two glutamic acid residues (E244 or E247) rendered full length maspin protein or 15-mer G-helix peptides inactive, in that they no longer could reduce cell migration or affect the actin cytoskeleton (Ravenhill *et al*. 2010).

In this work, we hypothesised that the effects of maspin on cellular behaviour would be reflected by changes in the cytoskeleton in a way that could be imaged and quantified. We used cell models with differential maspin exposure achieved by stable or transient transfection, or by the addition of recombinant protein or bioactive peptides. Images acquired from *in vitro* experiments were used to create a quantitative image analysis model of the cellular cytoskeleton using a hybrid marker controlled watershed segmentation technique. The insights into how maspin influences cytoskeletal architecture support the roles of maspin in the alteration of cell function.

MATERIALS AND METHODS

Cell Lines, Immunological Markers, Protein, Peptides

MCF-7 and DU145 cell lines with differing maspin expression generated and maintained as before (Ravenhill *et al.* 2010). Cell lines were authenticated by the DNA Diagnostics Centre (London, UK). Primary aortic smooth muscle cells (referred to as VSMC) were cultured as detailed previously (Bass *et al.* 2009). HT1080 were obtained from ATCC and maintained in Dulbecco's modified Eagle's medium (DMEM), supplemented with 10% (v/v) foetal calf serum (FCS). All cell culture reagents, Alexa Fluor 568 labelled phalloidin and secondary antibodies were from Life Technologies (Paisley, UK). Maspin peptides (Ravenhill *et al.* 2010) and recombinant maspin (Bass *et al.* 2009) as detailed previously. Commercially available mouse monoclonal antibodies were used to detect maspin (BD Biosciences, Oxford, UK). Control IgG was from Dako (Ely, UK).

Immunofluorescence Microscopy

Coverslips were coated with isolated ECM components at 5μg/ml for 15 hours at 4ºC. Cells were plated and incubated for 17 hours, then fixed as subconfluent monolayers with 4% formaldehyde and washed with PBS (phosphate buffered saline). For actin staining 0.2U of Alexa Fluor 568 labelled phalloidin was added to each sample and incubated in PBS for 40 minutes at room temperature. This was followed by two PBS washes. In some experiments cells were incubated with 10μM of individual maspin peptide or 100nM maspin in serum free conditions for up to 24 hours prior to staining. Slides were mounted with hydromount (National Diagnostics, GA, USA). Cells were visualised under a Charge Coupled Device (CCD) upright microscope or a LSM confocal microscope (Carl Zeiss Ltd, Hertfordshire, UK). Images were captured with Axiovision 4.7.1 software and Zeiss LSM Examiner 4.0. The real image sample is given as a figure 1, where three interested regions (nuclei, cytoplasm and ruffling region) are marked.

Image Processing

Generally, digital confocal microscopy images need a good segmentation method to allow cells to be segmented, even if they have grown in clumps or in a layered fashion. To date, there exists four major cell or cell nuclei segmentation approaches: global thresholding, adaptive thresholding, active contours and watershed segmentation techniques. Global thresholding is very simple and easy to tune, because it only works with non-overlapping cells or

nuclei. One disadvantage of thresholding is that it requires evenly distributed intensity backgrounds for analysis (Nyirenda *et al.* 2011). Adaptive thresholding is the improved version of thresholding; it requires varying window sizes across the image and adjusting threshold within each window for heterogeneous images (Zaritsky *et al.* 2011). The active contour method can identify object outlines in complex images, but it needs human intervention and supervision, as well as complex energy function (Wienert *et al.* 2011; Mueller *et al.* 2013). It provides a region - based and edge-based segmentation boundary approach, with parametric active contour (Zimmer & Olivo-Marin, 2005) to solve the problem of overlapping nuclei. Watershed segmentation is a powerful technique which can identify overlapping nuclei and solve the variable intensity and background problems (Wählby *et al.* 2004). Watershed alternatively means catchment basin, which can be defined as the region over which all points flow "downhill" to a common point. An alternative approach is to imagine the landscape being immersed in a lake, with holes pierced in local minima. Catchment basins will fill up with water starting at these local minima, and, at points where water coming from different basins would meet and dams are built. When the water level is reached the highest peak in the landscape, the process is stopped. As a result, the landscape is partitioned into regions or basins separated by dams, called watershed lines or simply watersheds. But under- and over- segmentation is a common problem of watershed segmentation, where a strong post-processing is needed to avoid this problem. Recently, several quantitative techniques were developed to quantify the subcellular structures like actin cytoskeleton, fibres like fibronectin, collagen; fractal based image analysis of actin cytoskeleton of neonatal cardiac fibroblast (Fuseler *et al.* 2007) and microvasculature in normal intestinal submucosa (Fuseler *et al.* 2010), quantification of immunostaining using digital image subtraction, blue filter and enhancement (DISBE) method (Bernardo *et al.* 2009) and automated podosome identification and characterization using segmentation and quantitative image modelling (Meddens *et al.* 2013). But to date, a complete segmentation technique is warranted for segmenting cellular cytoskeletal regions to identify variations in subcellular organisations from co-stained nuclei and cytoplasm image samples.

Marker controlled watershed segmentation (MCWS) is a watershed segmentation method in which initial makers need to be identified before the flooding process. The efficiency of MCWS depends on the selection of the right marker for the interested regions in a heterogeneous image; otherwise it may lead to over-segmentation problems. This can happen in the case of irregular shaped, overlapped or connected nuclei or cells. MCWS can restrict over-segmentation if the maker can represent the individual nuclei or cell. There are many reports of different algorithms

developed to identify good markers i.e. using minima of cell nuclei shape (Cheng and Rajapakse, 2009), distance transform algorithms (Lindblad *et al.* 2004; Jung and Kim, 2010), smart markers (Koyuncu *et al.* 2012). Alternatively, a post-processing routine can deal with over- and under-segmentation problems right after the segmentation process. To date, many post-processing algorithms have been developed, among them, region merging algorithm after segmentation (Ng *et al*. 2008), multi-scale and hierarchical segmentation (Cates *et al*. 2005) and image pre-processing before watershed segmentation (Lindblad *et al*. 2004; Sun & Luo, 2009; Plissiti *et al*.2011) are popular.

There are other methods available for segmenting the microscopic images such as K-means clustering, fuzzy c-means clustering and graph cuts. The K-means clustering is an iterative method used to partition an image into K clusters. First, it picks K clusters centers either randomly or based on some heuristic or probabilistic rule. Then, it assigns cluster labels to each pixel in the image that minimizes the distance between the pixel and the cluster center, and recomputes the cluster centers by averaging all the pixels in the cluster. It continues assigning and recomputing until convergence is attained or no pixel changes its cluster. Previously, K-means has been used for nucleus and cytoplasm detection using expectation maximisation algorithm (Sinha and Ramakrishnan, 2003), segmenting nucleus, cytoplasm, red blood cells and background (Mohapatra *et al*. 2011) and leukocyte segmentation (Ko *et al.* 2011). Fuzzy c-means uses partial membership of any data sample to all clusters in comparison to K-means. Fuzzy c-means is an iterative clustering method which produces an optimal partition by minimizing the weighting within a group sum of squared error objective function. It is now extensively used for cell segmentation purposes such as the segmentation of white blood cell (Umpon, 2005) and an automated leukocyte segmentation method for blood smear images (Ghosh *et al*. 2010). Recently, Fatima and Seenivasagam, (2011) presented a fast method to segment cells by executing initial segmentation using fuzzy c-means followed by the use of a watershed like method. Graph cut is another recent technique which is used to analyse blood cancer samples, where a concave vertex graph is constructed from the points and edges of automated detected concave area of the blood samples (Yang *et al.* 2008). Here, a hybrid approach of marker controlled watershed segmentation algorithm allowed us to segment the confocal complex microscopy images from *in vitro* assays. A summary of the quantitative image model is shown in figure 2. We computed descriptors to show resemblances between biological hypothesis and quantitative measures of the cellular cytoskeleton.

Initially, a pre-processing step was used to identify the cells lying from different contrasted background. Normally, confocal microscope images have uneven illumination and striped pattern problems which have to be corrected before doing any image analysis. Uneven illumination and striped pattern problems occur in some of the images due to the dust on the confocal slits. The image pre-processing must be done before segmenting the cell parts. Watershed segmentation is sensitive to the noise, as it can easily take any noise a catchment basin during the flooding process. Filtering helps to reduce noise and preserve the edges prior to applying the segmentation algorithm. After filtering the filtered image can be subtracted to see the performance of the filtering method. Here, we implemented three different filtering techniques: laplacian, gaussian and median filters to reduce the noise up to certain level, then we selected the appropriate filter option. First, we used a laplacian spatial filter which is a 2-D isotropic measure of the second spatial derivative of an image which highlights rapid intense changes in the image (Gonzalez & Woods, 1992). Gaussian filter is used `blur' images to remove detail and noise via 2-D convolution smoothing operator. We acquired the double stained images which gave separate nuclei image, both laplacian and Gaussian filters did not work very well in this case (shown in figure 3b and 3c) and after subtracting the filtered image from real nuclei image we can see the noise elimination was unsatisfactory (figure 3f & 3g). To make it precise we used a median filter. Basically, a median filter takes each pixel in the image in turn and considers its nearby neighbours to decide whether or not it is representative of its surroundings. Instead of simply replacing the pixel value with the mean of neighbouring pixel values, it replaces it with the median of those values. The median is calculated by first sorting all the pixel values from the surrounding neighborhood into numerical order and then replacing the pixel being considered with the middle pixel value. The intensity variation was resolved between the inside and the outside of the cells by image enhancement; by setting an adaptive intensity threshold value t_{adapt} and by applying an iterative median filtering with CLAHE algorithm (Zuiderveld, 1994). Intensity variation of background and foreground objects has been resolved by setting an adaptive intensity threshold value by applying CLAHE. The iterative process estimated background intensity while we used a median filter (shown in figure 3d) and subtracted from the real background (shown in figure 3h). The parameters used during median filtering in presented in table 1 .Raw images were subsampled by a factor 2 to speed up the processing. The subsampled image data sets had sufficient resolution to analyse for the details of image descriptors.

Step 1. Nuclei Segmentation

Before extracting any descriptors or information from the images, the cells needed to be identified as segmented objects with individual nuclei and surrounding cytoplasm. Each image contained several cells with single or combined nuclei, a cytoplasmic region and scattered ruffling regions. For segmentation, each cell was outlined by separating the nucleus and the cytoplasm. We deployed hybrid MCWS for nuclei and cytoplasmic segmentation. Nuclei segmentation was performed first to provide the seeds for the cytoplasmic segmentation. A detail process is given step by step in figure 4(a-h). We computed the gradient magnitude variation in the image. It produced a differential contrast between the foreground object bordered with the background (figure 4b). We used a sobel horizontal edge-emphasizing filter. We then applied morphological operations to develop good seeds for watershed segmentation. In between this process, 2 times dilation was needed to reconstruct the original nuclei size (shown in figure 3c). The small particle which was not related with the nuclei was removed as noise (figure 4d).

Clustered nuclei were separated by applying Euclidean distance transform (DT) to the binary image (Breu *et al.* 1995). Let $I : \Omega \subset \mathbb{Z} \rightarrow \{0,1\}$ be a binary image where the domain Ω is convex and, in particular, $\Omega = \{1,\dots,n\} \times \{1,\dots,n\}$, unless otherwise stated (Rosenfeld and Pfalz, 1968). Generally 0 is considered to black and 1 to white. Thus we have an object A is represented by all the white pixels:

$$A = \{p \in \Omega \mid I(p) = 1\} \qquad (1)$$

A is the foreground object and can consist of any subset of the image domain which includes disjoint sets also. A^c is the complement of A, defines the set of black pixels in Ω which is basically called background. The distance transform generates a map L whose value in each pixel p is the smallest distance form this pixel toA^c.

$$L(p) \coloneqq \min\{d(p,q) \mid q \in A^c\} = \min\{d(p,q) \mid I(q) = 0\} \qquad (2)$$

The image L is the distance map of A or *I*. Moreover $d(p,q)$is generally taken as Euclidean distance, given by equation 3.

$$d(p,q) = \sqrt{(p_x - q_x)^2 + (p_y - q_y)^2} \qquad (3)$$

The DT map is shown in figure 4e and *–Inf* is imposed on DT map in clear background in figure 4f. Touching nuclei were separated by applying watershed segmentation to the output of the distance transform image map (figure

4g). Borders were drawn to delineate the segmented nuclei using connecting neighbourhood points (figure h). Parameters used in nuclei segmentation steps are summarised in table 2.

Step 2. Cytoplasm Segmentation

After producing nuclei seeds, cytoplasm separation was needed to identify the ruffled pixels or intensities around the cells boundaries. Each image specimen contained several single and combined nuclei and cytoplasm. We used segmented nuclei as seeds in watershed segmentation of cytoplasm. First, the cytoplasm samples were filtered using median filter (figure 5a) and then we filled the cytoplasmic areas to identify the area without holes (figure 5b). To separate the touching cytoplasm we applied gray-weighted distance transform (GWDT) to the grayscale image (Fouard & Gedda, 2006). Before applying to the distance transform, we made a cytoplasm mask by applying extended minima transform with distance transform of nuclei, which is the regional minimum of the h-minima transform (Jung & Kim, 2010) (figure 5c). Let J denote the inverse distance map of clustered cytoplasm. The *h*-minima transform is performed by,

$$H_h(J) = R_J^{\varepsilon}(J + h) \qquad (4)$$

Where h represents the given depth and R and ε represent the reconstruction and erosion operators, respectively. Normally, all minima whose depth are lower than or equal to the given h-value are suppressed. The larger the h-value is, the fewer the numbers of the segmented regions. This step was crucial because once there was a good marker (figure 5c) for the gray-weighted distance transform; the algorithm could find the drainage regions for watershed flooding process (figure 5d & 5e). Then the watershed algorithm was applied to separate each cytoplasmic region (figure 5f). The boundaries of the watershed regions are arranged on the desired ridges, thus separating each object from its neighbours. The performance of watershed segmentation was dependent on the selection of right markers; otherwise it produced over segmentation. The parameter values used during cytoplasm segmentation is presented in table 3.

Step 3. Post-processing Method

In four datasets (fibronectin, laminin, collagen I and plastic) the illumination of the acquired image samples were not the same, due to this over-segmentation arose during the segmentation process. Sometimes the nuclei seeds were segmented perfectly, but the cytoplasm was not segmented due to over-segmentation. To reduce over-segmentation a post-processing algorithm was developed where the over-segmented samples were given as an input. We used a

region merging algorithm to avoid over- and under-segmentation which made our segmentation more adaptive. When the algorithm got the final segmented labelled image, it calculated the number of watershed flooded areas and retrieved them as sub-images with real intensity from the real image. We created an intensity pixel list where we could get the intensity values of labelled regions. If the algorithm found any small object, then it compared its intensity value with neighboring regions. If it found any single touching object then the label was put into a merging list. In the case of several touching objects, it took the highest summed intensity of touching objects to the merging list. When the merging list was ready, then objects were merged according to the merging list. Zero in the merging list represented objects that should be discarded as noise.

Step 4. Ruffling Area Extraction

Once we got the segmented nuclei and cytoplasm cellular parts, then we could define the actual cell areas within the image samples. The actual cell areas directed us to refine rest of the cell parts except nuclei and cytoplasm around the cell. We defined that region as ruffling regions around the cytoplasm that were outside the cytoplasmic area (shown in figure 1). To find the central massif we defined the exact cell cytoplasm boundary and converted the labelled matrix of segmented cytoplasm to grayscale image (figure 6a). We filled the gray-scale image and converted it into a binary image (figure 6b). We subtracted this from the cleaned binary image of the entire cell cytoskeleton image leaving the ruffling regions (figure 5c).Then the borders were drawn and superimposed on original cytoplasmic grayscale images (figure 5d).

Step 5. Descriptor Measurements

For calculating descriptors (Table 4) we needed to retrieve the original pixels of separated sub-images of nuclei, cytoplasm and ruffling regions from the main image samples. For retrieving the pixels of sub-images we used a technique described elsewhere (Srisukkham *et al.* 2013).

Cell Migration Assays

Cell migration was determined using time lapse video microscopy as described previously (Bass *et al.* 2009).

Affinity chromatography

An affinity column was used to identify cell proteins specifically binding to maspin as previously reported (Bass *et al.* 2009). To briefly reiterate HT1080 cell lysate from at least 60 x 10^6 cells was applied to a maspin affinity column. The column was incubated for 15 minutes at 25^{o}C and washed with PBS to remove unbound protein (wash

fractions 1-10). Protein bound to the column was eluted by the sequential application of PBS containing 0.5M NaCl (fractions 11-13), PBS containing 1M NaCl (fractions 14-16) and 0.1M sodium acetate/0.5M NaCl/pH4 (fractions 17-19). Fractions 20 & 21 resulted from further washing with PBS. Each fraction was concentrated 20-fold by trichloroacetic acid precipitation as previously described (Ravenhill *et al.* 2010) prior to SDS-PAGE. Gels were either stained with colloidal coomassie blue prior to excision of single bands for peptide mass fingerprinting (John Innes Centre Proteomic Facility, Norfolk, UK), or with coomassie blue and then silver stain according to the manufacturer instructions (Bio-Rad, Hemel Hempstead, UK).

In addition an affinity column was made with the isolated G-helix peptide (Ravenhill *et al.* 2010) using a 1-ml HiTrapTM NHS HP column (GE Healthcare) and 1 mg of peptide coupled to the column according to the product guidelines. Cell extracts were applied to the column and eluted as for the full length maspin column.

Statistical analysis

The statistical analysis was carried out with Minitab and Microsoft Excel. Data are presented as mean ± standard error of the mean (SEM). Significance was judged using Student's t-test and defined $P < 0.05$.

RESULTS

The ability of maspin to reduce cell migration is well documented by this group (Bass *et al.* 2002, 2009 Ravenhill *et al.* 2010) and others (Zou *et al.* 1994, Seftor *et al.* 1998, Sheng *et al.* 1996, Shi *et al.* 2001, 2007, Odero-Marah *et al.* 2003, Qin & Zhang 2010). The influence of maspin on the actin cytoskeleton consistent with these functional effects has also been reported, both in terms of the rearrangements of actin filaments because of maspin status (Odero-Marah *et al.* 2003, Qin & Zhang 2010, Lara *et al.* 2012) and effects on the expression of proteins that control cytoskeletal rearrangement (Odero-Marah *et al.* 2003, Chen *et al.* 2005). We have previously reported that the actin cytoskeleton reflects the reduction of cell migration observed in cells transfected with maspin, or with the G-helix peptide that mimics the effect of full length maspin added (Ravenhill *et al.* 2010). Here we sought to model the relationship between maspin and actin to provide quantitative measurements and to investigate the nature of the interactions between maspin and actin in our cell models.

Image Analysis of Transfected MCF-7

An illustration of the image analysis process is provided (Figure 2); the analyses were performed on images of differently transfected MCF-7 cells where the nuclei had been stained with DAPI and the actin cytoskeleton with phalloidin. Two channel image acquisitions allowed us to supply nuclei and whole cell images to the nuclei and cytoplasm segmentation algorithms respectively. Nuclei segmentation was fundamental prior to the segmentation of the cytoplasm, because good nuclei markers were used as seeds for the cytoplasmic segmentation. After segmenting the cytoplasm, ruffling areas were extracted. The cells inside the image samples were different in nature; some samples had only single nuclei, some had clumped or combined nuclei and cytoplasm. The whole segmentation section was divided into 5 subsections (Figure 2): nuclei segmentation, cytoplasm segmentation with seeded nuclei, image post-processing, ruffling region extraction and descriptor measurements.

During the segmentation process, some parameters were varied to get good segmentation quality. The parameters used during the segmentation processes are summarised in table 1, 2 and 3. In the pre-processing stage, the method used subsampled images which were done using ImageJ software LOCI toolbox (ImageJ, 2014). In the case of median filtering, the median value was given in the (3, 3) neighborhood around the corresponding pixel in the input image. During the nuclei segmentation process, morphological operation was implemented where the thresholded image was dilated. After the morphological operation euclidean distance transform was applied and a mask was

made from the output of DT by applying h-minima transform which made a good mask for identifying the position of nuclei (Figure 2, step 1). Then the DT map and mask were superimposed to get a good mask before applying the watershed. After making the mask, watershed was applied while watershed successfully finds the basin of the nuclei. Then individual nuclei were separated with border.

Once the method had the nuclei seeds, the cytoplasm segmentation algorithm took seeded nuclei to find the accurate position of the cytoplasm by using extended h-minima transform (Figure 2, step 2). After that the GWDT was applied with the mask of seeded nuclei, before that median filter was used to the cytoplasm. Then the method superimposed the GWDT map to the mask, which revealed the watershed catchment basin lines. Then the watershed was applied to separate the single or clumped cytoplasm and a boundary was drawn. In the case of over-segmentation, the over-segmented cells were supplied to a post-processing algorithm to allow correction (Figure 2, step 3). After the nuclei and cytoplasm were separated, then the ruffling regions were extracted (Figure 2, step 4). A summary of all individual ECM components: collagen I, fibronectin, laminin and plastic cellular segmentation is given in supplementary figure S1.

We used this hybrid quantitative image model to successfully put together a novel protocol for the analysis of images of the co-stained cells which allowed us to model the effects of maspin using images of almost 500 cells, extending the scope and reliability of the study. A number of parameters were measured (Figure 2, step 5) that generally supported the hypothesis that maspin expressing cells have morphology consistent with being less motile than cells which do not express maspin. The effects of growing cells on different ECM components and the requirement for an intact G-helix varied.

Quantitative Measures of Cellular Cytoskeleton Structure

MCF-7 stably transfected to express maspin show a significant reduction in cell migration as measured by time lapse video microscopy, in comparison to MCF-7 containing an empty vector control or a E244A maspin mutant (Figure 7a). This was the case for cells grown on plastic, fibronectin and collagen I. In the presence of laminin the reduction in migration caused by maspin was maintained in the presence of the E244A mutation. The area measurements were generally in good agreement with the measured migration. The area occupied by MCF-7 cells expressing wild type maspin was decreased in comparison to control cells by as much as 65% (Figure 7b). When grown on plastic, fibronectin and laminin the cells expressing E244A mutant maspin were the same as the control cells, indicating a

reliance on an intact G-helix for how maspin was altering cell morphology. The reduction in area in cells expressing maspin was consistent with a contracted, less motile morphology.

A decrease in the area of the ruffling region in all cells expressing maspin was observed in comparison to control cells (Figure 7c); most dramatically a 10-fold difference in cells grown on fibronectin. This was consistent with maspin expressing cells being less motile, but did not require an intact G-helix. EFF provides a measure of how near cells are to an epithelial shape (Figure 7d). An epithelial cell will have an EFF of 1. Here when we consider cells grown on plastic, cells containing maspin proteins are more epithelial in shape than those that do not express it. On the matrix components the story is less clear, which implies that engagement with the ECM is a stronger signal than the presence or absence of maspin. Only on laminin do maspin expressing cells show a more epithelial like shape than control cells and this difference is small although significant.

Changes in the Actin Cytoskeleton Caused By Maspin and Maspin Peptides

The pattern of the actin cytoskeleton was determined by staining F-actin with Alexa Fluor 568 phalloidin in cells transfected stably or transiently with maspin, or with exogenously added maspin protein or peptides. This was done with MCF-7 breast cancer and DU145 prostate cancer cell lines, as well as primary human VSMC, all of which do not express maspin but which have been shown to respond to maspin (Bass *et al.* 2002, Yin *et al.* 2005, Ravenhill *et al.* 2010, Liao *et al.* 2014). All cells showed a rearrangement of the actin cytoskeleton in the presence of maspin, which indicated the universal nature of these effects.

MCF-7 cells were stably transfected with pcDNA-3.2 (Figure 8a, d, g, j), pcDNA3.2-Maspin (Figure 8 b, e, h, k) or pcDNA-E244A (Figure 8 c, f, i, l) and grown sparsely on isolated ECM components: plastic control (Figure 8 a-c), laminin (LN, Figure 8 d-f), collagen I (CNI, Figure 8 g-i) or fibronectin (FN, Figure 8 j-k). These cells migrated at different rates depending on their maspin status; MCF7 -pcDNA-3.2 at 4.9±3.6μm/hr, MCF-7-pcDNA3.2-Maspin at 1.8±1.2μm/hr, MCF7-pcDNA-3.2-E244A at 4.1±2.2μm/hr (Ravenhill *et al.* 2010). The presence of wild type maspin caused a >60% reduction in MCF-7 migration which should be reflected in the cytoskeletal architecture. MCF7-pcDNA-3.2 (Figure 8 a, d, g, j), cells had the short actin filaments and thin lamellipodia characteristic of a motile cell. MCF-7-pcDNA3.2-Maspin (Figure 8 b, e, h, k) had a more regular cell shape with a decrease in thin membranous extensions and cortical actin around the entire cell periphery; consistent with the cells being less motile (Ridley *et al.* 2003). The MCF7-pcDNA-3.2-E244A (Figure 8 c, f, i, l) cells expressing a maspin protein with a

mutation in E244A of the G-helix had a cytoskeleton architecture that fell between these two extremes. The cells expressing the mutant maspin showed thick peripheral actin-rich lamellipodia that could be seen around the cell circumference in a non-polarised manner. But these had a thin diameter and showed increased ruffling with frequent membrane protrusions. The expression of wild type maspin in MCF-7 influenced the re-organisation of the actin cytoskeleton consistent with the reported reduction in migration (Ravenhill *et al.* 2010).

DU145 were transiently transfected with pcDNA-3.2 (Figure 8m) or pcDNA3.2-Maspin (Figure 8n) and again demonstrated actin structures consistent with a reduction in migration in the presence of maspin. DU145-pcDNA-3.2 (Figure 8m, migration rate 2.3±1.3μm/hr (Ravenhill *et al.* 2010) showed numerous long, thin, filopodia extending from the basal cell surface into the surrounding environment. Filopodia extended from the entire cell periphery and formed thin intercellular bridges with adjacent cells. In comparison DU145 pcDNA3.2-Maspin (Figure 8n, migration rate 1.6±1.0μm/hr (Ravenhill *et al.* 2010) showed intercellular bridges, yet the frequency and length of filopodia were reduced; specifically at the periphery where neighboring cells were not present. Maspin expressing cells showed a replacement of thin protrusions with thick focal adhesion like structures at the cell edge.

DU145 cells incubated in the presence of maspin peptides for 24 hours showed a different pattern of cytoskeletal staining depending on whether they had been exposed to the scrambled control peptide (Figure 8o, migration rate 3.3±1.8μm/hr (Ravenhill *et al.* 2010), the wild type G-helix peptide (Figure 8p, migration rate 1.8±1.0μm/hr (Ravenhill *et al.* 2010) or the G-helix with the E244A mutation peptide (Figure 8q, migration rate 2.4±1.3μm/hr (Ravenhill *et al.* 2010). DU145 cells incubated with G-helix peptide (Figure 8p) showed a rounded phenotype with an increased actin cortex often exhibiting lamellipodia structures around the whole of the cell, as observed with MCF-7-pcDNA3.2-Maspin (Figure 8 b, e, h, k). G-helix treated cells showed a marked decrease in filopodia and radial organisation of stress fibres at the cell edge; all indicating that these cells were not migratory. Cells treated with either mutant G-helix peptide E244A (Figure 8q) or control peptide (Figure 8o) showed longer central stress fibres and multiple membrane protrusions often forming directed lamellipodia, indicating that these cells were motile. Thus the effect of wild type maspin protein on the re-organisation of the actin cytoskeleton was mimicked by a peptide spanning its wild type G-helix. Similarly, the inability of mutant maspin protein E244A to promote actin reorganisation and functional modification was mimicked by the E244A peptide. This indicated the importance of the G-helix of maspin in the rearrangement of the actin cytoskeleton.

Adding recombinant maspin to the media of VSMC also changed the appearance of the actin cytoskeleton (Figure 8 r-t). Generally there was an increase in cell body size on maspin treatment and a reduction in the number of filopodia; the cells showed elongated stress fibres indicating that the cell were less motile in the presence of maspin, as we have functionally demonstrated before (Bass *et al.* 2002). Control VSMC had more membrane spikes and shorter stress fibres, which is consistent with more motile cells. The changes in the actin cytoskeleton of VSMC were visible after a short incubation (Figure 8s), after 24 hours there was an increase in the thickness of membrane protrusions (Figure 8t).

We have previously shown that maspin delivered by transfection, or by the addition of proteins or isolated G-helix peptides reduces migration (Bass *et al.* 2002, Ravenhill *et al.* 2010). Here we show that this is reflected in the actin cytoskeleton and that the effects of maspin on migration and in the reflected cytoskeletal rearrangements are disrupted by mutations in the G-helix.

Identification of Maspin and G-Helix Binding Cellular Proteins

Affinity columns were used to identify proteins binding to full length, wild type maspin (Figure 9a & b) or the isolated G-helix peptide (Figure 9c & d). We used HT1080 cells for these experiments to generate the large cell numbers required for the affinity column experiments and downstream mass spectrometry analyses. The HT1080 cell lysate was applied to each column and specifically bound proteins were eluted under stringent conditions (high (NaCl) and low pH). Three proteins were specifically eluted from the maspin column (Figure 9b) and four proteins from the G-helix column (Figure 9d). Peptide mass fingerprinting identified that five different proteins were being eluted from the columns (Table 5), with β-actin and cognate hsp70 were being specifically eluted from both columns.

DISCUSSION

The link between the effects of maspin on cell behaviour and cytoskeletal architecture has been reported before (Odero-Marah *et al.* 2003. Qin & Zhang 2010. Lara *et al.* 2012). This study extends the observations beyond cells transfected stably or transiently with maspin, to those with added recombinant maspin or bioactive peptides of a region previously demonstrated to affect cell migration. In addition to imaging the cytoskeleton, we developed a novel computer model that allowed quantitative measurements of the changes in cell shape on addition of maspin proteins. Insights into how maspin influences cytoskeletal arrangements were provided by demonstrations of maspin – actin binding. Overall we demonstrate that the appearance of the cellular cytoskeleton was affected by maspin status in a way that could be linked to migratory potential of the cells. We demonstrate that the changes in cellular actin patterns upon exposure to maspin were the same in widely different cell types, arguing that maspin has impact on fundamental mechanisms that regulate cell shape and motility.

Looking at the patterns of the actin cytoskeleton in MCF-7, DU145 and VSMC exposed to maspin proteins or G-helix peptides we saw a common theme. The cytoskeletal architecture of the cells exposed to full-length maspin or the G-helix in isolation reflected a less motile phenotype, with longer thicker actin filaments. Our visual observations were supported by migration data and the image analyses, which generally fitted the model whereby maspin expressing cells showed a morphology suggesting a less motile phenotype. A direct consideration of cell area provided the most powerful indication of the effects of maspin on cell morphology and so behaviour. Maspin expressing MCF-7 showed a reduced cell area in comparison to control cells and those expressing mutant maspin.. Cells expressing wild type or E244A mutant maspin were found to have a decreased ruffling region in comparison to control cells on all matrix components, again consistent with a less motile phenotype in the presence of maspin. When it came to EFF the maspin expressing cells were only measured to be more epithelial in the absence of exogenously added ECM; cells grown on ECM were not significantly altered by maspin. Although cells grown in the absence of added ECM are actually synthesising fibrillar matrix, this implies that engagement with the exogenous ECM provided a stronger signal than the presence or absence of maspin.

The circularity of cells was calculated, such that a perfectly round cell would have a circularity of 1. If the area of a cell did not alter this would mean that as cells became more motile, the periphery would increase and so the

circularity decrease indicting a motile phenotype. Since the area of the cells altered (Figure 8a) this linear interpretation was not valid and changes in circularity could not be directly linked to cell shape and motility. Similarly density index was calculated, this related area and perimeter, which as both alter here makes it difficult to interpret. These parameters are not reported in detail as they did not provide useful insight.

To evaluate the segmentation accuracy, we used manual software to crop original nuclei and cytoplasm manually, and then compared with the segmented nuclei and cytoplasm obtained from our proposed segmentation methods. For measuring the similarity we used correlation coefficient, R. Normally, R varies from -1 to 1, values closer to 1 means the cropped nuclei or cytoplasm had more conformity with the segmented images of the proposed method and vice versa. The images we investigated were divided into four groups according to the ECM components: plastic, fibronectin, laminin and collagen I. We measured the segmentation accuracy of two segmentation algorithms for each dataset (Table 6). The results show the slightly more significant accuracy for nuclei segmentation algorithms than cytoplasm algorithms in the case of four datasets. Normally, the segmentation accuracy of the cytoplasm algorithms depended on the nuclei segmentation accuracy, because segmented nuclei seeds had been supplied as a maker for the cytoplasm segmentation algorithm. For fibronectin and laminin the segmentation accuracy is almost same in the range (R = (0.95-0.96)), but for plastic the nuclei segmentation is greater than cytoplasm. This happened because for some image samples there was uneven illumination. But overall, our segmentation algorithms showed a good performance. It is worth to mention that the proposed algorithm will work for other cellular cytoskeletal image datasets, where co-staining has been used.

The segmentation methods used in this paper have some limitations which need to be considered. The accuracy of cytoplasm segmentation was completely depended on the right seeded nuclei mask obtained from nuclei segmentation. In the case of cells on plastic, the DT map of nuclei did not perform very well because of uneven contrast during data acquisition, as a result the segmentation accuracy varied for cells on plastic. This depended on the success of extended h-minima transform during the making of markers for nuclei segmentation. If the method could not avoid the tiny dots from the background (which were due to noise), it created an over segmentation. In case of more than two clumped cytoplasmic areas, the performance of GWDT was around 80%, we did not have many clumped cytoplasms where there was more than two cytoskeleton areas. Especially, in cells on plastic the cytoskeleton structures were unevenly contrasted, but for collagen, laminin and fibronectin the algorithm segmented the clumped nuclei quite successfully. Surprisingly, our nuclei segmentation algorithm segmented the clumped

nuclei (more than two) successfully for all the datasets. Another limitation is that the method could not deploy any classification techniques, as there is no benchmark data for this research domain, especially focused to the cellular cytoskeletal changes due to maspin with co-stained images. These limitations will be investigated thoroughly by the use of different image processing techniques in future.

Using affinity columns the binding of cell proteins to full length maspin or the G-helix in isolation was determined and five proteins identified as binding one or both columns. In this way we demonstrated a direct interaction between maspin and β-actin. The interaction between maspin and actin has been reported previously (Cella *et al.* 2006) and also contended (Teoh *et al.* 2014). This study supports the presence of an interacting relationship between maspin and actin. Of the other maspin-binding proteins identified here, only hsp70 has been reported elsewhere (Yin *et al.* 2005); this is a chaperone protein so is likely to be binding in this capacity. PDI P5 (protein disulphide isomerase P5) is a disulphide isomerase and chaperone. Members of the PDI family were thought to be resident in the endoplasmic reticulum, but increasingly are reported on the cell surface with roles in receptor conformation alteration and shedding (reviewed by Jordan & Gibbins 2006). An interaction between maspin and PDI P5 is intriguing, especially if that interaction were to be on the cell surface. ATP synthase α & β subunits have been shown to interact with another member of the serpin family; placental epithelial derived factor (Notari *et al.* 2010, Deshpande *et al.* 2012) with roles in the inhibition of angiogenesis and tumor cell proliferation, but the interaction has not been investigated in relation to maspin to date.

Summary

In conclusion, the present work has combined the development of a novel image analysis technique based on mathematical modelling of cytoskeletal architecture with multiple cell biology approaches. We demonstrate that the effects of maspin or bioactive peptides of maspin on cell migration are mirrored by effects on cell architecture, and that the G-helix is a key bioactive part of the molecule.

References

Al-Mamun MA, Brown LJ, Hossain MA, Fall C, Wagstaff L & Bass R. (2013). A hybrid computational model for the effects of maspin on cancer cell dynamics. *Journal of Theoretical Biology*, 337, 150 – 160.

Bass R, Moreno Fernandez AM & Ellis V. (2002) Maspin inhibits cell migration in the absence of protease inhibitory activity. *Journal of Biological Chemistry*, 277(49), 46845-46848.

Bass R, Wagstaff L, Ravenhill L & Ellis V. (2009) Binding of extracellular maspin to beta1 integrins inhibits vascular smooth muscle cell migration. *Journal of Biological Chemistry* 284(40), 27712-20.

Bass R, Werner F, Odintsova E, Sugiura T, Berditchevski F & Ellis V. (2005) Regulation of urokinase receptor proteolytic function by the tetraspanin CD82. *Journal of Biological Chemistry* 280(15), 14811-8.

Bernardo V, Lourenço SQ, Cruz R, Monteiro-Leal LH, Silva LE, Camisasca DR, Farina M, Lins U, (2009). Reproducibility of immunostaining quantification and description of a new digital image processing procedure for quantitative evaluation of immunohistochemistry in pathology. *Microsc Microanal*. 2009 Aug;15(4):353-65.

Bodenstine TM, Seftor RE, Khalkhali-Ellis Z, Seftor EA, Pemberton PA, & Hendrix MJ. (2012). Maspin: molecular mechanisms and therapeutic implications. *Cancer and Metastasis Reviews*. 31(3-4), 529-51.

Breu H, Gil J, Kirkpatrick D, & Werman M. (1995). Linear time Euclidean distance transform algorithms. *IEEE Transactions on Pattern Analysis and Machine Intelligence* 17, 529–533.

Cella N, Contreras A, Latha K, Rosen JM, & Zhang M. (2006). Maspin is physically associated with (beta)1 integrin regulating cell adhesion in mammary epithelial cells. *FASEB Journal* 20(9), 1510-2.

Chen EI, Florens L, Axelrod FT, Monosov E, Barbas CF 3rd, Yates JR 3rd, Felding-Habermann B & Smith JW. (2005). Maspin alters the carcinoma proteome. *FASEB Journal* 19,1123-1124.

Cheng J & Rajapakse JC. (2009). Segmentation of clustered nuclei with shape markers and marking function. *IEEE Transactions on Biomedical Engineering* 56(3), 741–748.

Fatima, MM. and Seenivasagam V. (2011). A fast fuzzy-c means based marker controlled watershed segmentation of clustered nuclei. In: *Proceedings of International Conference on Computer, Communication and Electrical Technology*.

Fenistein D, Lenseigne B, Christophe T, Brodin P & Genovesio A. (2008), A fast, fully automated cell segmentation algorithm for high-throughput and high content screening, *Cytometry Part A* 73(10), 958–964.

Fuseler JW, Millette CF, Davis JM & Carver W. (2007). Fractal and image analysis of morphological changes in the actin cytoskeleton of neonatal cardiac fibroblasts in response to mechanical stretch. *Microscopy and Microanalysis*, 13, 133–143.

Fuseler JW, Bedenbaugh A, Yekkala K, Baudino TA.(2010). Fractal and image analysis of the microvasculature in normal intestinal submucosa and intestinal polyps in Apc(Min/+) mice. Microsc Microanal Feb;16(1):73-9.

Fouard C, & Gedda M. (2006). An objective comparison between grey weighted distance transforms and weighted distance transforms on curved spaces, discrete geometry for computer imagery. *Lecture Notes in Computer Science* Volume 4245, pp 259-270.

Ghosh M, Das D, Chakraborty C, & Ray AK. (2010). Automated leukocyte recognition using fuzzy divergence. *Micron* 41, 840–846.

ImageJ (2014). http://www.openmicroscopy.org/site/support/bio-formats5/ users/ imagej/ (Accessed on 20/05/2014)

Jordan PA, & Gibbins JM. (2006). Extracellular disulfide exchange and the regulation of cellular function. *Antioxidants and Redox Signaling* 8(3-4), 312-24.

Jung C & Kim C. (2010). Segmenting clustered nuclei using h-minima transform-based marker extraction and contour parameterization, IEEE *Transactions on Biomedical Engineering*, Vol. 57, No. 10.

Ko BC, Gim J, & Nam J. (2011). Automatic white blood cell segmentation using stepwise merging rules and gradient vector flow snake. *Micron* 42, 695–705.

Koyuncu CF, Arslan S, Durmaz I, Cetin-Atalay R, & Gunduz-Demir C. (2012). Smart markers for watershed-based cell segmentation. *PLoS One* 7(11), e48664.

Lara H, Wang Y, Beltran AS, Juárez-Moreno K, Yuan X, Kato S, Leisewitz AV, Cuello Fredes M, Licea AF, Connolly DC, Huang L, & Blancafort P. (2012). Targeting serous epithelial ovarian cancer with designer zinc finger transcription factors. *Journal of Biological Chemistry* 287(35), 29873-86.

Liao XH, Li YQ, Wang N, Zheng L, Xing WJ, Zhao DW, Yan TB, Wang Y, Liu LY, Sun XG, Hu P, Zhou H, & Zhang TC. (2014). Re-expression and epigenetic modification of maspin induced apoptosis in MCF-7 cells mediated by myocardin. *Cellular Signaling* 26(6):1335-46.

Lindblad J, Wählby C, Bengtsson E, & Zaltsman A. (2004). Image analysis for automatic segmentation of cytoplasms and classification of Rac1 activation, *Cytometry Part A.* 57(1), 22-33.

Lindblad J, & Bengtsson EA. (2001). Comparison of methods for estimation of intensity nonuniformities in 2D and 3D microscope images of fluorescence stained cells. *In Proceedings of the 12th Scandinavian Conference on Image Analysis (SCIA)*, Bergen, Norway. p264–271.

McCormack SA, Ray RM, Blanner PM, & Johnson LR. (1999). Polyamine depletion alters the relationship of F-actin, G-actin, and thymosin beta4 in migrating IEC-6 cells. *American Journal of Physiology* 76(2 Pt 1), C459-68.

Meddens MB, Rieger B, Figdor CG, Cambi A, van den Dries K. (2013). Automated podosome identification and characterization in fluorescence microscopy images. *Microsc Microanal.* Feb;19(1):180-9.

Mohapatra S, Patra D, & Satpathy S. (2011). Automated leukemia detection in blood microscopic images using statistical texture analysis. In: *Proceedings of International Conference on Communication, Computing; Security.*

Mueller JL, Harmany ZT, Mito JK, Kennedy SA, Kim Y, Dodd L, *et al.* (2013). Quantitative segmentation of fluorescence microscopy images of heterogeneous tissue: application to the detection of residual disease in tumor margins. *PLoS One* 8(6), e66198.

Notari L, Arakaki N, Mueller D, Meier S, Amaral J, & Becerra SP. (2010). Pigment epithelium-derived factor binds to cell-surface F(1)-ATP synthase. *FEBS Journal.* 277(9), 2192-205.

Ng HP, Ong SH, Foong KW, Goh PS, & Nowinski WL. (2008). Masseter segmentation using an improved watershed algorithm with unsupervised classification, *Computers in Biology and Medicine* 38(2), 171-84.

Nyirenda, N., Farkas, D. L. & Ramanujan, V. K. (2011). Preclinical evaluation of nuclear morphometry and tissue topology for breast carcinoma detection and margin assessment', *Breast Cancer Research and Treatment* 126(2), 345–354.

Odero-Marah, V.A., Khalkhali-Ellis, Z., Chunthapong, J., Amir, S., Seftor, R.E., Seftor, E.A., & Hendrix, M.J. (2003). Maspin regulates different signaling pathways for motility and adhesion in aggressive breast cancer cells. *Cancer Biology and Therapy* 2, 398-403.

Pham TD. (2008). Fuzzy Fractal Analysis of Molecular Imaging Data, *Proceedings of the IEEE*, vol.96, no.8, pp.1332, 1347.

Plissiti ME, Nikou C, & Charchanti A (2011). Combining shape, texture and intensity features for cell nuclei extraction in pap smear images. *Pattern Recognition Letters* 32, 838–853.

Qin L, & Zhang M. (2010). Maspin regulates endothelial cell adhesion and migration through an integrin signaling pathway. *Journal of Biological Chemistry* 285(42), 32360-9

Rao JY, Hurst RE, Bales WD, Jones PL, Bass RA, Archer LT, Bell PB, & Hemstreet GP 3rd. (1990). Cellular F-actin levels as a marker for cellular transformation: relationship to cell division and differentiation. *Cancer Research* 50(8),2215-20.

Ravenhill L, Wagstaff L, Edwards DR, Ellis V & Bass R. (2010) The G-helix of maspin mediates effects on cell migration and adhesion. *Journal of Biological Chemistry* 285(47), 36285 - 92.

Ridley AJ, Schwartz MA, Burridge K, Firtel RA, Ginsberg MH, Borisy G, Parsons JT, & Horwitz AR. (2003). Cell migration: integrating signals from front to back. *Science* 302(5651), 1704-9.

Seftor RE, Seftor EA, Sheng S, Pemberton PA, Sager R, & Hendrix MJ. (1998). Maspin suppresses the invasive phenotype of human breast carcinoma. *Cancer Research* 58(24), 5681-5.

Sheng S, Carey J, Seftor EA, Dias L, Hendrix MJ, & Sager R. (1996). Maspin acts at the cell membrane to inhibit invasion and motility of mammary and prostatic cancer cells. *Proceedings of the National Academy of Sciences USA* 93(21), 11669-74.

Shi HY, Stafford LJ, Liu Z, Liu M, & Zhang M. (2007). Maspin controls mammary tumor cell migration through inhibiting Rac1 and Cdc42, but not the RhoA GTPase. *Cell Motility and the Cytoskeleton* 64(5), 338-46.

Shi HY, Zhang W, Liang R, Abraham S, Kittrell FS, Medina D, & Zhang M. (2001). Blocking tumor growth, invasion, and metastasis by maspin in a syngeneic breast cancer model. *Cancer Research*, 61, 6945–6951.

Sinha N, & Ramakrishnan AG. (2003). Automation of differential blood count. In: *Proceedings of TENCON Conference on Convergent Technologies for Asia-Pacific Region.*

Sun HQ, & Luo YJ. (2009). Adaptive watershed segmentation of binary particle image, *Journal of Microscoscopy*. Feb;233(2), 326-30.

Srisukkham W, Lepcha P, Hossain MA, Zhang L, Jiang R, & Lim HN. (2013). A Mobile Enabled Intelligent Scheme to Identify Blood Cancer for Remote Areas - Cell Membrane Segmentation using Marker Controlled Watershed Segmentation Phase. *In The 7th International Conference on Software, Knowledge, Information Management and Applications (SKIMA)*, 18-20 Dec, Chiang Mai, Thailand.

Teoh SS, Vieusseux J, Prakash M, Berkowicz S, Luu J, Bird CH, Law RH, Rosado C, Price JT, Whisstock JC, & Bird PI. (2014). Maspin is not required for embryonic development or tumor suppression. *Nature Communications* 5, 3164.

Teera-Umpon N. (2005). Patch-based white blood cell nucleus segmentation using fuzzy clustering. *ECTI Trans. Electr. Electron. Commun*. 3, 5–10.

Wählby C, Sintorn IM, Erlandsson F, Borgefors G and & Bengtsson E. (2004). Combining intensity, edge and shape information for 2D and 3D segmentation of cell nuclei in tissue sections. *Journal of Microscoscopy* 215(Pt 1), 67–76.

Weichsel J, Herold N, Lehmann MJ, Kräusslich HG & Schwarz US. (2010), A quantitative measure for alterations in the actin cytoskeleton investigated with automated high-throughput microscopy, *Cytometry Part A* 77(1), 52–63.

Wienert S, Heim D, Saeger K, Stenzinger A, Beil M, Hufnagl P, Dietel M, Denkert C & Klauschen F. (2011). Detection and segmentation of cell nuclei in virtual microscopy images: a minimum-model approach. *Scientific Reports* 2, 503.

Yang L, Tuzel O, Meer P, & Foran D. (2008). Automatic image analysis of histopathology specimens using concave vertex graph. In *Proc. Med. Image Comput. Comput.-Assist. Interv.*, New York, NY, USA, 2008, 833–841.

Yin S, Li X, Meng Y, Finley RL Jr, Sakr W, Yang H, Reddy N, & Sheng S. (2005). Tumor-suppressive maspin regulates cell response to oxidative stress by direct interaction with glutathione S-transferase. *Journal of Biological Chemistry* 280(41), 34985-96.

Zaritsky A, Natan S, Horev J, Hecht I, Wolf L, *et al.* (2011). Cell motility dynamics: a novel segmentation algorithm to quantify multi-cellular bright field microscopy images. *PLoS One* 6(11), e27593.

Zimmer, C. & Olivo-Marin, J. C. (2005). Coupled parametric active contours. *IEEE Transactions on Pattern Analysis and Machine Intelligence* 27(11), 1838–1842.

Zou Z, Anisowicz A, Hendrix MJ, Thor A, Neveu M *et al.* (1994). Maspin, a serpin with tumor-suppressing activity in human mammary epithelial cells. *Science* 263(5146), 526–529.

Zuiderveld K. (1994). Contrast limited adaptive histogram equalization. Graphics gems IV, *Academic Press Professional, Inc* 474–485.

Table Legends

Table 1 – Parameters values used during the image pre-processing step

Table 2 – Parameter values of nuclei segmentation steps

Table 3 – Parameter values of cytoplasm segmentation steps

Table 4 - Descriptors of cellular morphology

Table 5 - Identification of proteins eluted from full length and isolated G-helix of maspin affinity columns

Table 6 – The measured segmentation accuracy for nuclei, cytoplasm and ruffling region algorithms by calculating the correlation coefficient (R).

Figure Legends

Figure 1- Raw subsampled confocal image marked with regions (nuclei, cytoplasm and ruffling regions) in a cell image obtained from confocal microscope.

Figure 2- Schematic overview of Quantitative image modelling of cellular cytoskeleton due to the effects of maspin

A schematic of the processes of nuclei segmentation (Step 1), cytoplasm segmentation (Step 2), post-processing (Step 3), ruffling area extraction (Step 4) and descriptor measurement (Step 5) is shown.

Figure 3- Three filtering methods were applied to the nuclei image to reduce the noise, a & e represents the real nuclei images, the first row (b-d) represent the output of three filtering methods laplacian, gaussian and median respectively. f- h show the subtracted filtered image from the real image for three filtering methods laplacian, gaussian and median.

Figure 4- The steps of nuclei segmentation. a) The pre-processed nuclei after pre-processing step, b) the gradient magnitude variation of background and border, c) after applying the morphological opening, d) removing small objects size 400 pixels, e) distance transform map of nuclei, f) the DT applied into *–Inf* background, g) watershed segmentation with gray labelled and h) drawn boundary with nuclei filled body.

Figure 5- The steps of cytoplasm segmentation. a) pre-processing with median filter of cytoplasm stained image sample, b) filled the whole of cytoplasmic area, c) imposing the nuclei seed as a mask using extended-minima transform, which is the regional minima of the H-minima transform level 5, d) GWDT of the grayscale cytoplasm

where the ask is true seed locations, e) the GWDT applied into *–Inf* background, f) labelled object after applying watershed segmentation, g) impose the segmented cytoplasmic parts with border to the real grayscale image and h) both nuclei and cytoplasm border were imposed.

Figure 6- The steps of ruffling regions extraction. a) segmented cytoplasmic parts with labelled , b) filled areas, c) subtract the filled area from grayscale cytoplasm sample and d) cytoplasm borders have been drawn over grayscale cytoplasm sample.

Figure 7 – Migration and parameter measurement by image analysis of MCF-7 cells

a) Migration of MCF-7 over ECM was measured over 18 hours and is presented as percentage migration relative to controls. MCF-7 migration as reported previously (Ravenhill *et al*. 2010) b) The area of cells was determined by quantification of pixels in each cell body c) Ruffling was calculated from the integrated intensity of the ruffling regions d) EFF was given by the ration of cell breadth to length.

In all cases the analysis of MCF-7-pcDNA3.2 (open bars), MCF-7-pcDNA3.2-Maspin (closed bars) and MCF-7-pcDNA3.2-E244A (hatched bars) are shown. For b) – d) at least 80 of each cell type were analysed (20 per ECM condition). * $p < 0.005$.

Figure 8– The architecture of the actin cytoskeleton influenced by maspin status

The actin cytoskeleton was stained with Alexa Fluor 568-labeled phalloidin in formaldehyde fixed MCF-7, DU145 and VSMC exposed to maspin in different ways. MCF-7 cells were stably transfected with pcDNA-3.2 (a, d, g, j), pcDNA3.2-Maspin (b, e, h, k) or pcDNA-E244A (c, f, i, l) and grown on isolated ECM components: plastic control (a-c), laminin (LN d-f), collagen I (CNI g-i) or fibronectin (FN j-k). DU145 were transiently transfected with pcDNA-3.2 (m) and pcDNA3.2-Maspin (n), or incubated with 10μM of control (o), G-helix (p) or E244A (q) peptide for 24 hours. VSMC were incubated with 100nM of recombinant maspin for 0 (r), 1 (s) or 24 (t) hours. Images obtained by confocal microscopy.

Staining performed on at least three independent samples, representative images selected.

Figure 9 – HT1080 cell proteins binding to affinity columns of full length maspin or the isolated G-helix

Cell lysate was applied to the affinity columns, after incubation the columns were washed with PBS to remove unbound protein (fractions 1-10). Eluates were collected by sequential application of 0.5M NaCl (fractions 11-13),

1M NaCl (fractions 14-16), pH4 (fractions 17-19) and PBS (fractions 20 -21). 1ml fractions were collected, TCA precipitated, combined with Laemmli sample buffer and separated by SDS-PAGE. Samples from the maspin column were visualised by coomassie blue (a) wash fraction b) eluates). Samples from the G-helix column were visualised by silver stain(c) wash fraction d) eluates). Bands specifically eluted and identified by peptide mass fingerprinting indicated by *.

Figure 1

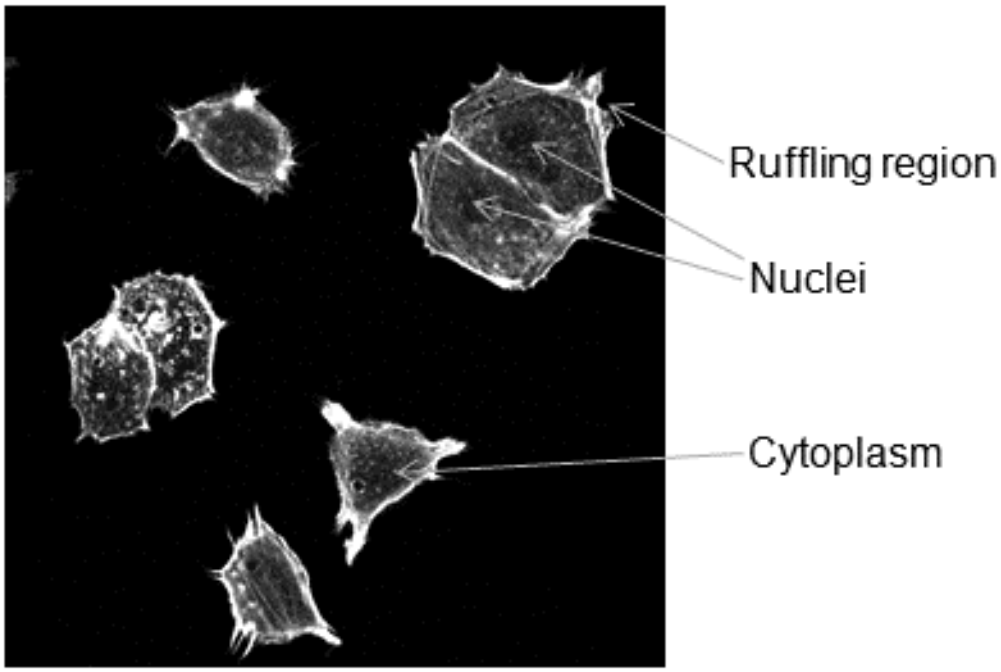

Figure2

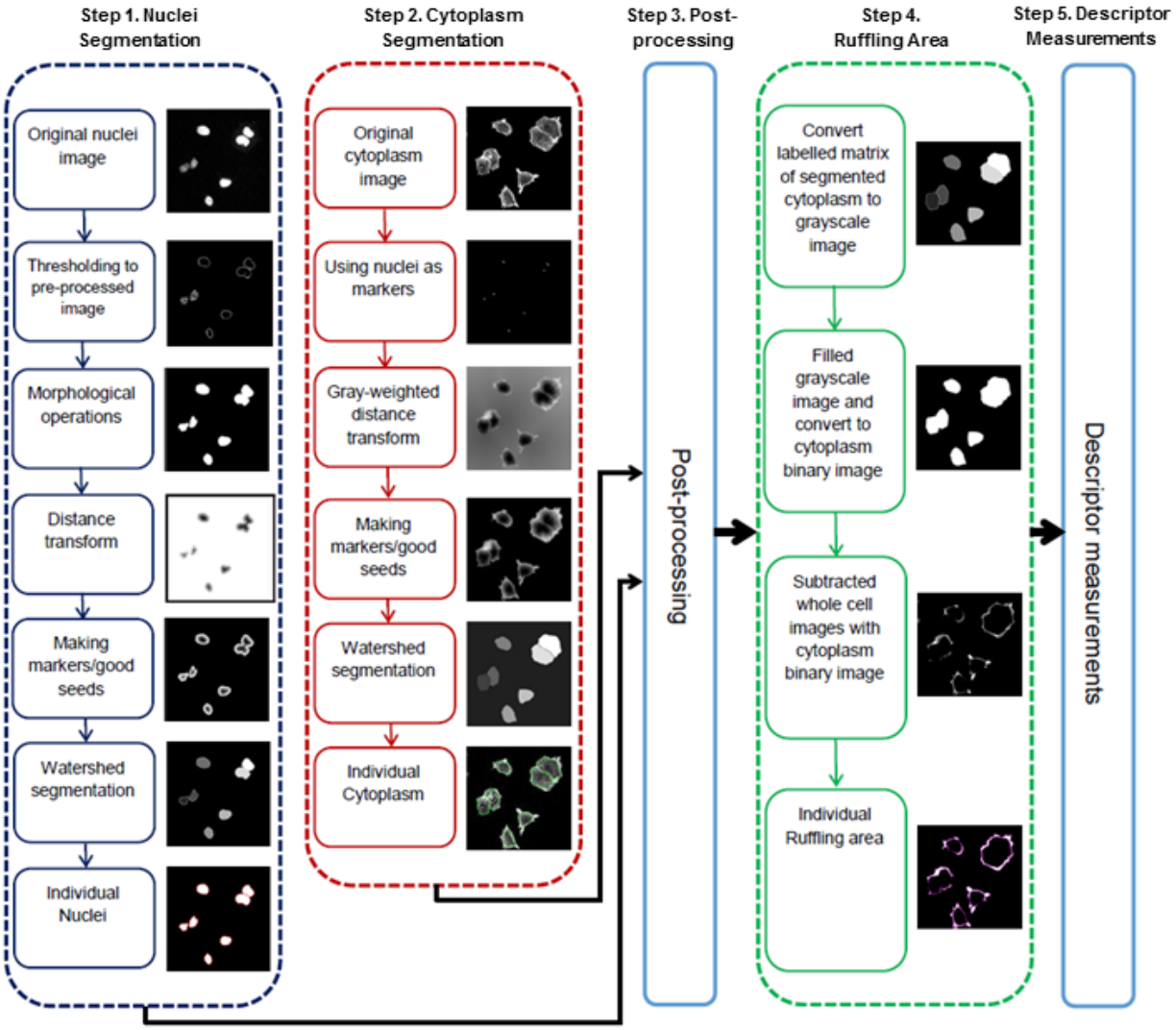
Step 1. Nuclei Segmentation
Original nuclei image
Thresholding to pre-processed image
Morphological operations
Distance transform
Making markers/good seeds
Watershed segmentation
Individual Nuclei
Step 2. Cytoplasm Segmentation
Original cytoplasm image
Using nuclei as markers
Gray-weighted distance transform
Making markers/good seeds
Watershed segmentation
Individual Cytoplasm
Step 3. Post-processing
Post-processing
Step 4. Ruffling Area
Convert labelled matrix of segmented cytoplasm to grayscale image
Filled grayscale image and convert to cytoplasm binary image
Subtracted whole cell images with cytoplasm binary image
Individual Ruffling area
Step 5. Descriptor Measurements
Descriptor measurements

Figure 3

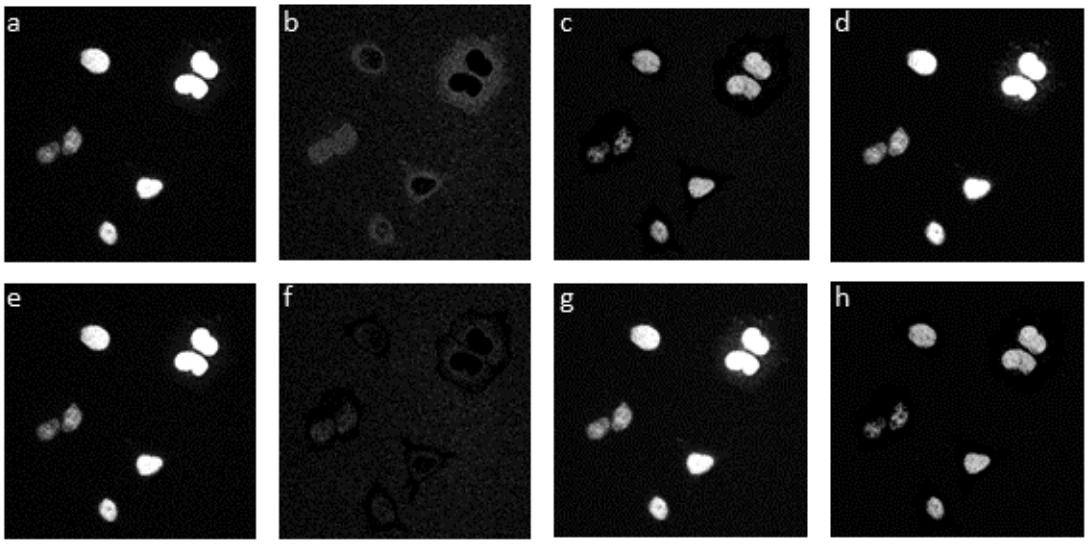

Figure 4

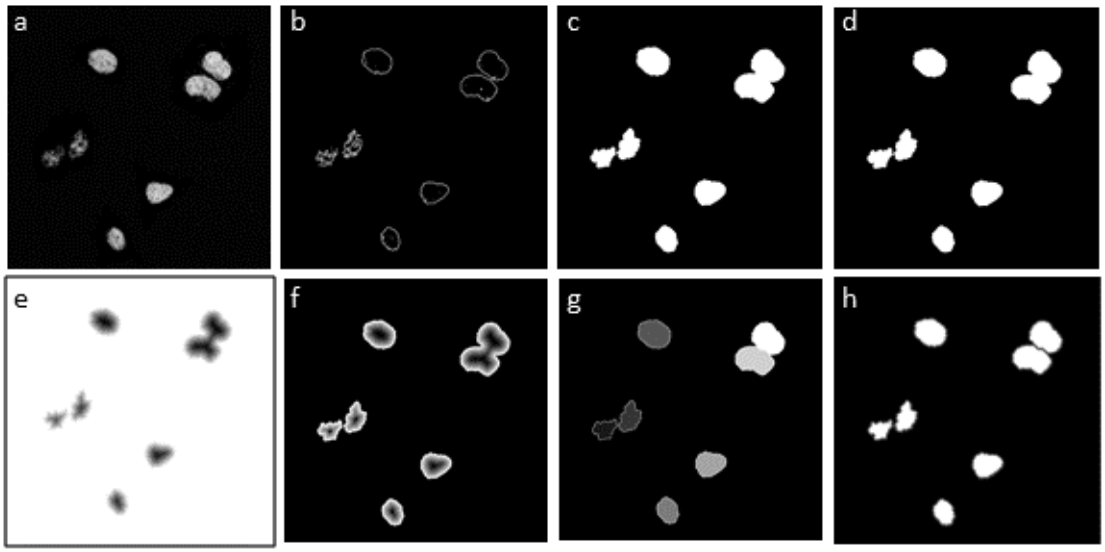

Figure 5

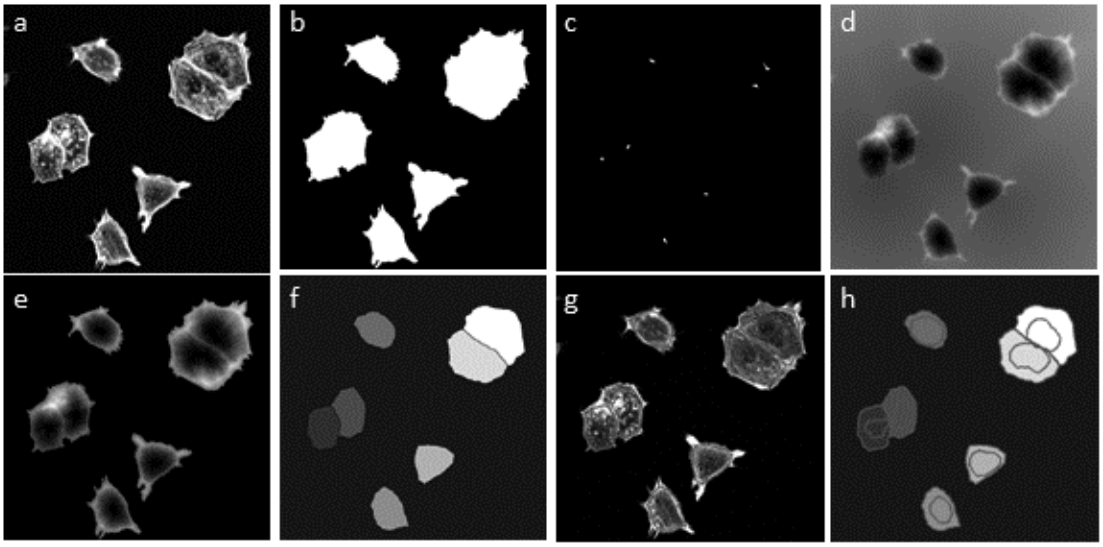

Figure 6

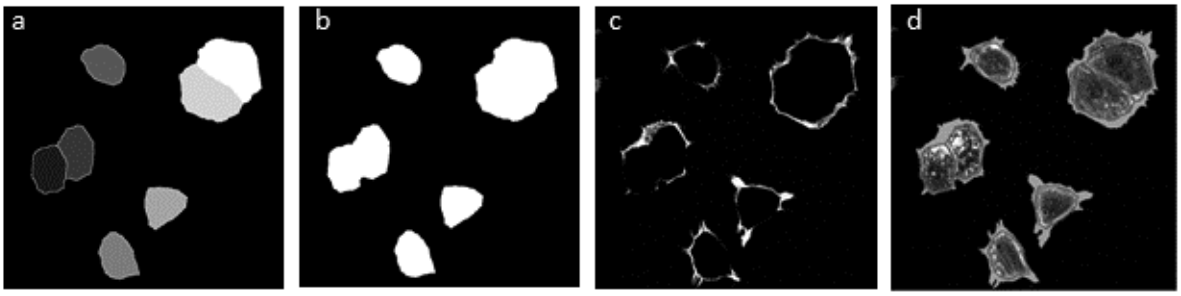

Figure 7

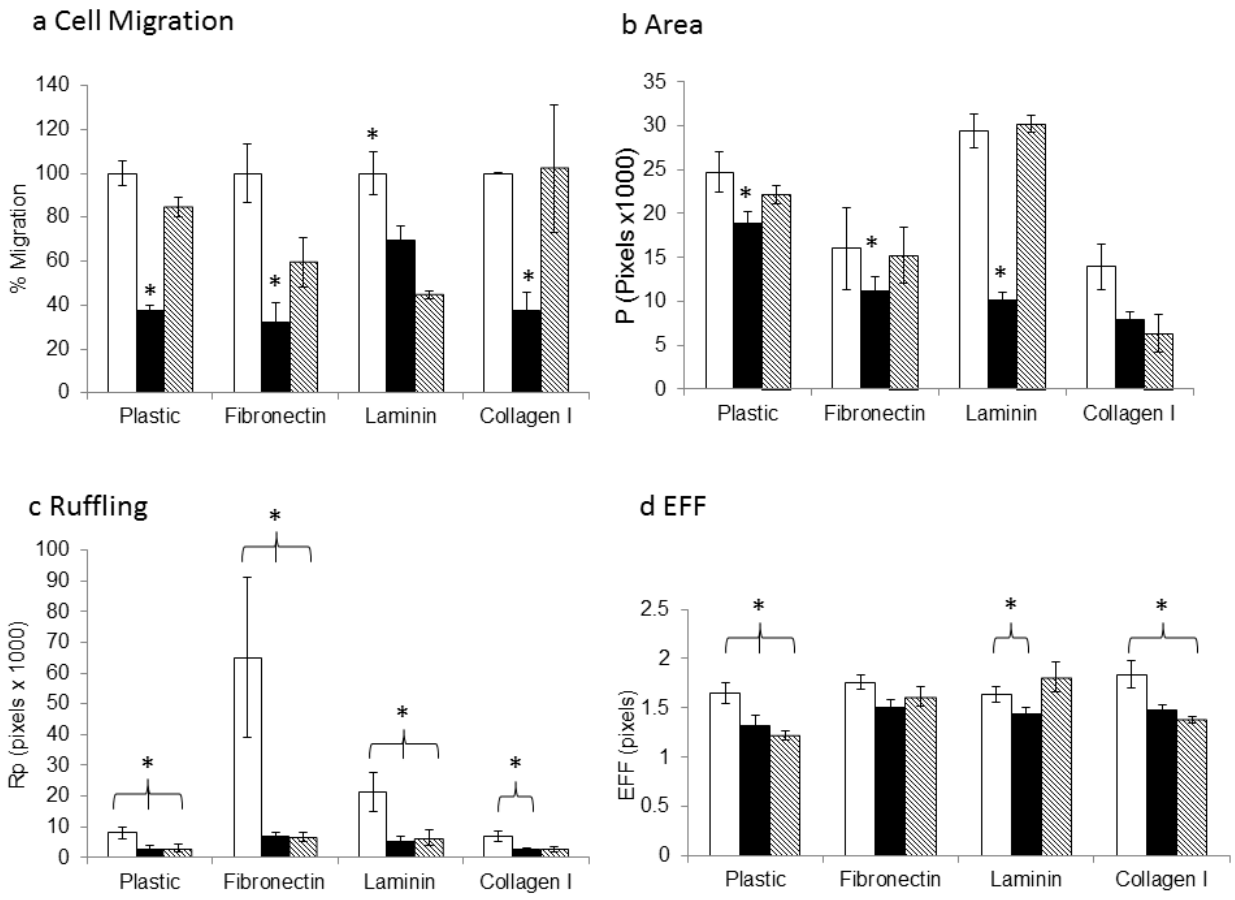
a Cell Migration
% Migration
140
120
100
80
60
40
20
0
Plastic
Fibronectin
Laminin
Collagen I
b Area
P (Pixels x1000)
35
30
25
20
15
10
5
0
Plastic
Fibronectin
Laminin
Collagen I
c Ruffling
Rp (pixels x 1000)
100
90
80
70
60
50
40
30
20
10
0
Plastic
Fibronectin
Laminin
Collagen I
d EFF
EFF (pixels)
2.5
2
1.5
1
0.5
0
Plastic
Fibronectin
Laminin
Collagen I

Figure 8

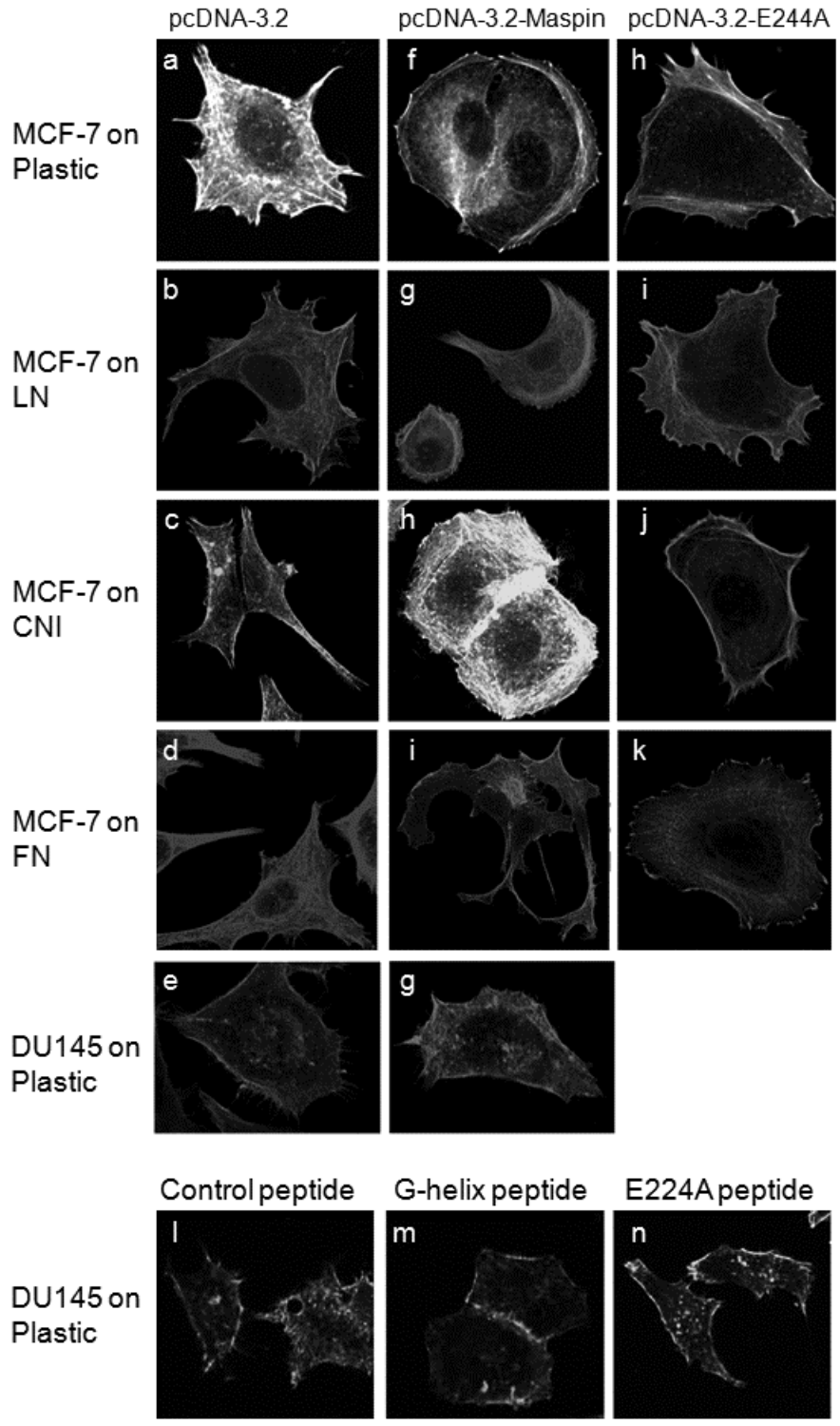
pcDNA-3.2
pcDNA-3.2-Maspin
pcDNA-3.2-E244A
MCF-7 on Plastic
MCF-7 on LN
MCF-7 on CNI
MCF-7 on FN
DU145 on Plastic
Control peptide
G-helix peptide
E224A peptide
DU145 on Plastic
a
f
h
b
g
i
c
h
j
d
i
k
e
g
l
m
n

Figure 9

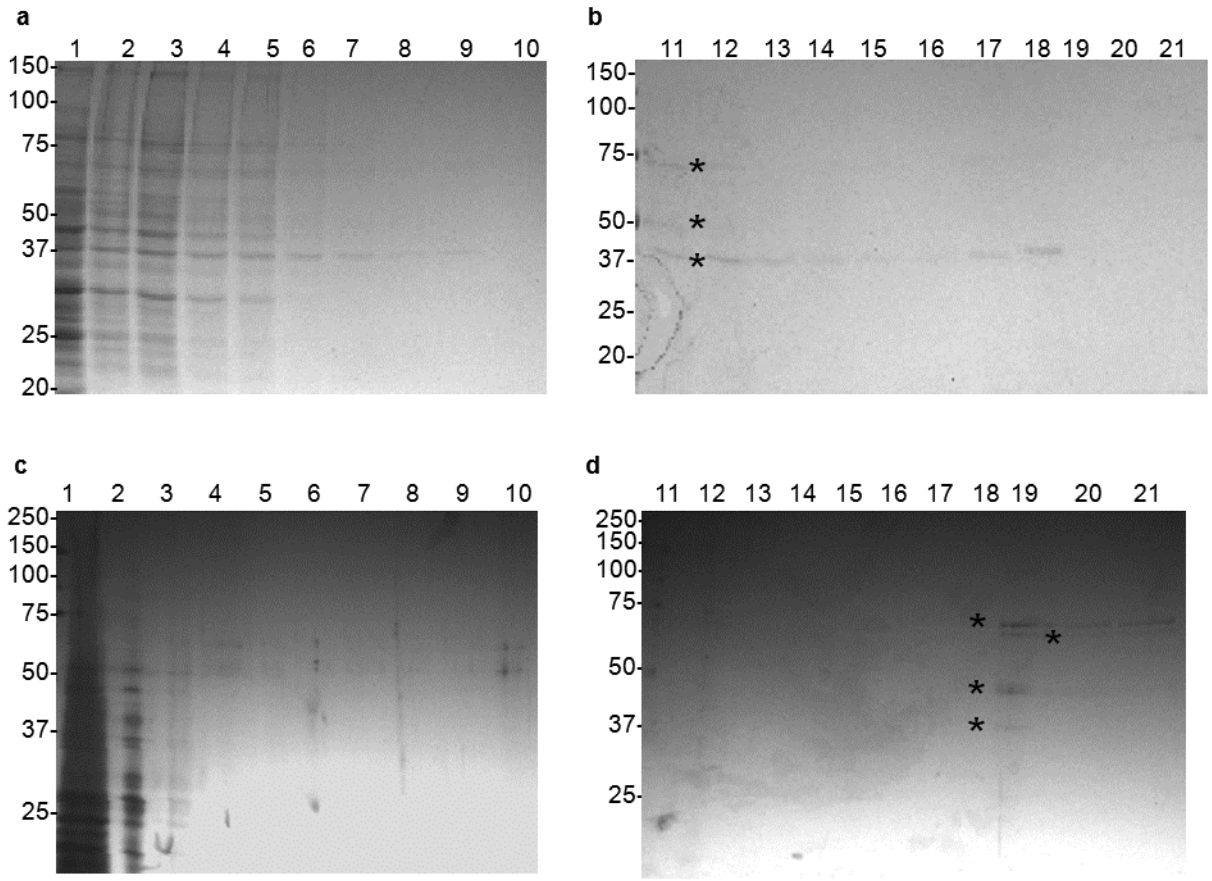
a
1 2 3 4 5 6 7 8 9 10
150
100
75
50
37
25
20
b
11 12 13 14 15 16 17 18 19 20 21
150
100
75
50
37
25
20
*
*
*
c
1 2 3 4 5 6 7 8 9 10
250
150
100
75
50
37
25
d
11 12 13 14 15 16 17 18 19 20 21
250
150
100
75
50
37
25
*
*
*
*

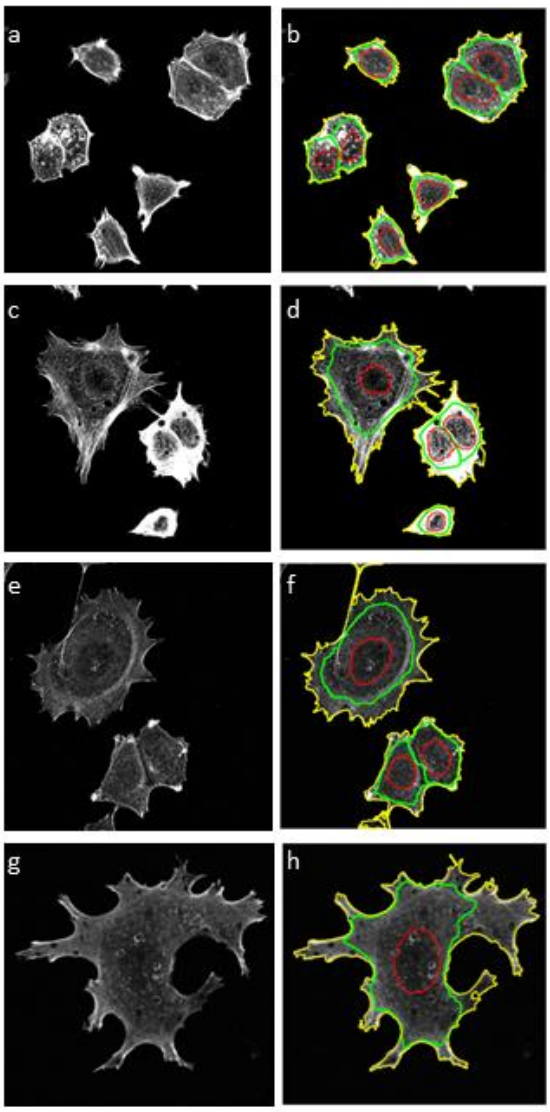

Figure S1: MCF 7 cells grown on individual ECM components: a) & b) collagen I, c) & d) fibronectin, e) & f) laminin and g) & h) plastic. The whole cell images are shown (a, c, e, g) alongside the results of segmentation (b, d, f, h). Nuclei are marked by red, surrounded by the green cytoplasm boundary and the whole cell body is marked by yellow boundary. The ruffling region is the inner region between the cytoplasm (green) and boundary of cell (yellow).